M3LW-24OR0402025

Light Water Reactor Sustainability Program

Advanced microstructural and electrochemical quantification of irradiated stainless steels

Xin Chen[1], Marta Pozuelo[1], Ashutosh Jangde[1], Maxim Gussev[2], Gaurav Sant[1]

[1]University of California, Los Angeles
[2]Oak Ridge National Laboratory

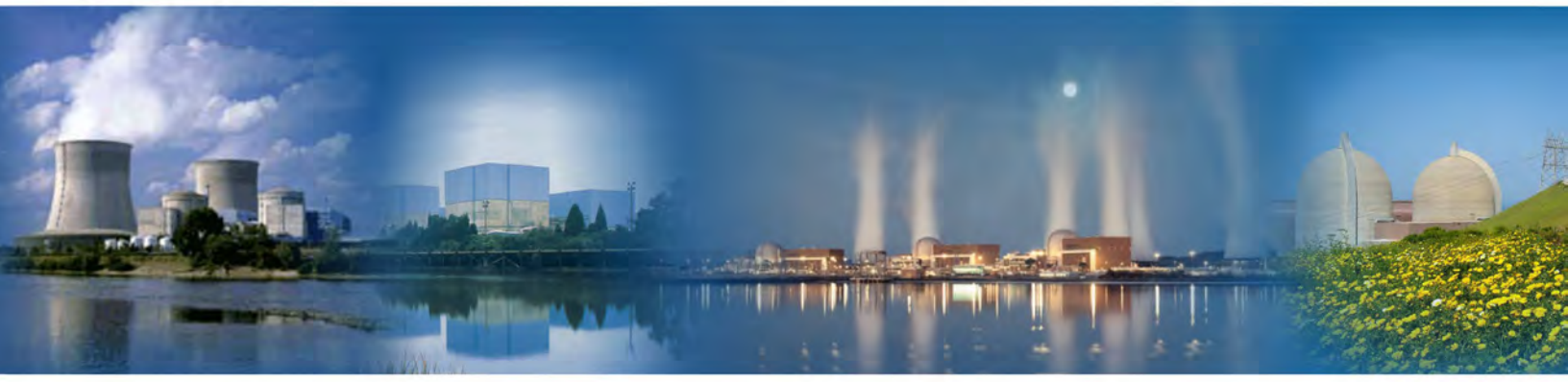

September 2024

U.S. Department of Energy

Office of Nuclear Energy

M3LW-24OR0402025

Advanced microstructural and electrochemical quantification of irradiated stainless steels

Xin Chen[1], Marta Pozuelo[1], Ashutosh Jangde[1], Maxim Gussev[2], Gaurav Sant[1]

[1]University of California, Los Angeles
[2]Oak Ridge National Laboratory

September 2024

Light Water Reactor Sustainability
Materials Research Pathway

Prepared for the
U.S. Department of Energy
Office of Nuclear Energy

Page intentionally left blank

ABSTRACT

There is a need for high-throughput, scale-relevant, and direct electrochemical analysis to understand the corrosion behavior and sensitivity of nuclear materials that are exposed to extreme (high pressure, temperature, and radiation exposure) environments. We demonstrate the multi-scale, multi-modal application of scanning electrochemical cell microscopy (SECCM) to electrochemically profile corrosion alterations in nuclear alloys in a microstructurally resolved manner. Particularly, we identify that both mechanically deformed and irradiated microstructures show reduced charge-transfer resistance that leads to accelerated oxidation. We highlight that the effects of mechanical deformation and irradiation are synergistic, and may in fact, superimpose each other, with implications including general-, galvanic-, and/or irradiation activated stress-corrosion cracking. Taken together, we highlight the ability of non-destructive, electrochemical interrogations to ascertain how microstructural alterations result in changes in the corrosion tendency of a nuclear alloy: knowledge which has implications to rank, qualify and examine alloys for use in nuclear construction applications.

Page intentionally left blank

ACKNOWLEDGEMENTS

The authors acknowledge financial support for this research provided by the U.S. Department of Energy's Light Water Reactor Sustainability (LWRS) Program Materials Research Pathway through the Oak Ridge National Laboratory operated by UT-Battelle LLC (Contract #: 4000154999) and The National Science Foundation (CAREER Award: 1253269, CMMI: 1401533). This research was carried out in the Laboratory for the Chemistry of Construction Materials (LC2) and the Electron Microscopy Core Facility at UCLA, and the Oak Ridge National Laboratory (ORNL). This manuscript has been authored in part by UT-Battelle, LLC under Contract No. DE-AC05-00OR22725 with the United States Department of Energy. The ion irradiation was performed at the Center for Integrated Nanotechnologies, an Office of Science User Facility operated for the U.S. Department of Energy (DOE) Office of Science. Los Alamos National Laboratory, an affirmative action equal opportunity employer, is managed by Triad National Security, LLC for the U.S. Department of Energy's NNSA, under contract 89233218CNA000001. As such, the authors gratefully acknowledge the support that has made these facilities and their operations possible.

CONTENTS

FIGURES

TABLES

Page intentionally left blank

Advanced microstructural and electrochemical quantification of irradiated stainless steels

1. Introduction

Forecasting the evolution of irradiation -assisted stress corrosion cracking (IASCC) remains challenging due to the unresolving issues in understanding the microstructure-corrosion interplay across scales. For this reason, many recent developments of scanning electrochemical cell microscopy (SECCM) technologies have resolved the scale limits imposed by conventional methods[1–3]. For instance, by using a micropipette to confine corrosion evaluation in a nano- to micrometer sized microdroplets, SECCM readily resolves small microstructural features[2,4–6]. The scanning probe technique has been consequently applied to study the mechanism of IASCC. For instance, in a previous study, we have demonstrated that surface electrochemical reactivity is correlated with strain-induced heterogeneities (e.g., martensite, point defects and dislocations) in austenitic stainless steels, even though these features are identical in composition with the austenitic matrix.[7] In addition, many other studies have reveal that, corrosion can be accelerated not only by plastic strain-induced microstructures, but can also activated by elastic stresses [8–11].

Akin to the deformation damage, irradiation also induces microstructural defects[12], which results in accelerated surface oxidation in nuclear reactor environments[13]. In both cases, irradiation and mechanical deformation increase the chemical reactivity in similar manners, i.e., by inducing defected phase-transformation (e.g., martensitic transformation)[14,15] or building stored energy in lattices[16,17]. This is significant since the enhancement of reactivity (oxidation tendency) is linked to the chemical potential (embodied by surface reactivity) that is in turn affected by mechanical deformation (i.e., effective plastic strain, EPS) and irradiation (i.e., displacement per atom, dpa). Based on these linkages, herein, we develop an electrochemical post-damage examination (Ec-PDE) approach to achieve multiscale, multimodal analyses on deformed and irradiated nuclear materials.

2. Experimental

2.1 Sample preparation

A hot rolled 304L stainless steel (ArcelorMittal) with the nominal composition listed in **Table 1** was sectioned into miniature tensile specimens shown in **Figure 1a**[18,19]. In deformation tests, two specimens were respectively elongated to a 30% strain and fracture under uniaxial tension at a strain rate of 5×10^{-4} s^{-1}. To make samples for SECCM, each sample was attached to a copper wire, and then embedded in epoxy resin. The exposed surfaces were successively polished (N.B., using the 50 nm colloidal silica as the final step) until the surface featured a mean-roughness S_a < 10 nm. After polishing, the samples were stored in a desiccator before used.

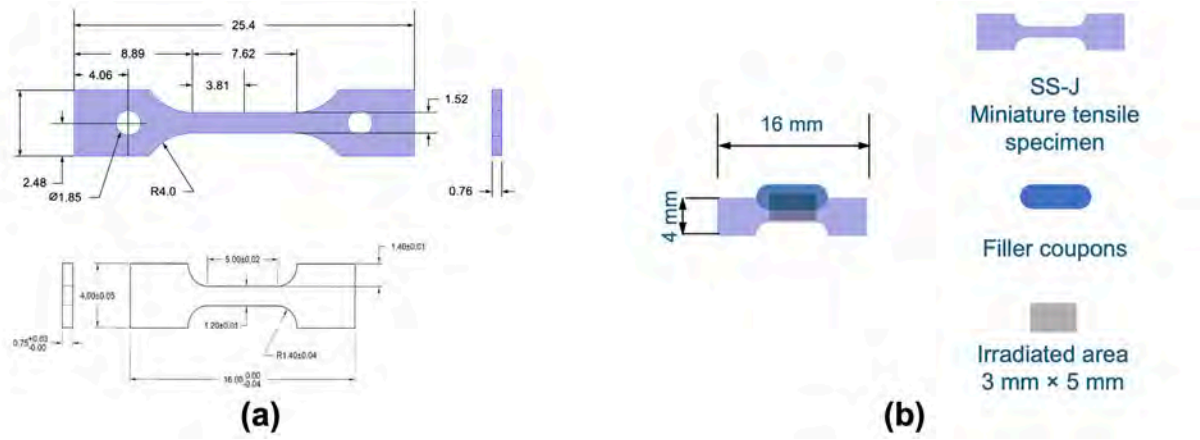

Figure 1. (a) Schematics of the miniature tensile samples used for (top) deformation and (bottom) H+-implantation. All values are in mm. (b) Schematics show the assembly irradiated under in the H+-implantation.

Table 1. The chemical composition of the 304L stainless steel used (mass %).

Fe	Cr	Ni	Mo	Mn	N	C	Si
71.82	18.29	8.02	0.07	1.28	0.05	0.02	0.45

2.2 Irradiation

A 304L steel tensile specimen and a spacer (see **Figure 1**) was annealed at 1050 °C for 3 h to produce solution-treated monophasic austenitic microstructure, with a grain size on the order of tens of micrometers. The specimens were partially irradiated at 300 °C by using a 1.5 MeV proton ($[H^+]$) beam (generated by the NEC 3 MV tandem ion accelerator, LLNL) until a target fluence of 1.84×10^{19} ions/cm^2 was attained. A flat-region irradiation damage level of 1.11 dpa was calculated based on full-cascade SRIM simulations[20]. Thereafter, the tensile specimen was elongated to a 1% strain under uniaxial tension at a strain rate of 5×10^{-4} s^{-1}. Additional 304L samples were also irradiated with other ion sources, three tensile specimens were irradiated using 5 MeV $[Fe^{++}]$ to a target of 1, 3, and 5 dpa (flat region).

2.3 Microstructural characterization

The crystallographic orientations of the grains were studied using a Scanning Electron Microscopy (SEM, Tescan Mira3) equipped with an electron backscatter diffraction detector (EBSD, Oxford Ultim Max). The acceleration voltage and step size used were 20 kV and 500 nm, respectively. The EBSD data were subsequently analyzed using the OIM Analysis® software.

A cross-sectional thin slide from the irradiated and deformed surface was prepared using Focused Ion Bean (FIB) ablation. An FEI Nova 600 Nanolab Dual-Beam Focused Ion Beam - Scanning Electron Microscope (FIB-SEM) was used for this purpose. The morphology and composition of three irradiated Stainless Steel (SS) samples were characterized by scanning electron microscopy (SEM) using a FEI Nova 230 Variable Pressure SEM (VP-SEM) equipped with a Thermo Fisher Scientific Electron Dispersive Spectroscopy (EDS) system.

High resolution transmission electron microscopy (HRTEM) was used to investigate the dislocation channels (DCs) and other defects such as stacking faults and twins found in the microstructure. A FEI Titan 300-kV scanning transmission electron microscope (STEM) was used for this purpose and a FEI Nova 600 Nanolab Dual-Beam Focused Ion Beam - Scanning Electron Microscope (FIB-SEM) was utilized for the TEM sample preparation. Different phases and layers of different compositions were identified with different contrast using bright field (BF), dark field (DF) and high-angle annular dark field (HAADF) detectors under the STEM mode. EDS mapping conducted in the Titan confirmed the composition of each layer.

Vickers hardness indentations were performed under a load of 200 gram force (gf) and loading time of 15s, 20 indentations were made 100 μm apart across the irradiated and unirradiated regions of the spacer.

2.4 Scanning probe analysis

The surface reactivity of the deformed and $[H^+]$-irradiated 304L steels were evaluated using a scanning electrochemical microscope (HEKA ElProScan, see **Figure 2a**). The instrument is equipped with micropipettes with a 1.8 ± 0.3 μm opening to probe spatially resolved electrochemical responses (see **Figures 2b-c**). The micropipettes were made at 700 °C by a pipette puller (Sutter P-1000), using filamented borosilicate glass tubes (1 mm ID, 1.5 mm OD). The SECCM tests were performed with the micropipettes filled with 0.2 M LiCl or 0.2 M LiCl + 5% HNO_3 solutions. N.B., Lithium is commonly used in pressurized water reactors (PWRs) as a coolant additive, therefore, LiCl as a potential coolant contaminant[21], was used to promote measurable corrosion signals; and the 0.2 M LiCl + 5% HNO_3 solution are used to dissolve surface hydroxides and reveal the corrosion resistance of only the protective "barrier" oxides. During scanning, the steel samples were connected as the working electrode and an AgCl-coated silver wire (Ag/AgCl) were inserted in the micropipette to serve as the quasi-reference-counter-electrode (QRCE). As the micropipette approached the steel surface, a 30s open circuit hold was performed allowing the microdroplets to stabilize and the open circuit potentials (OCP) were measured at the end of the hold. Thereafter, potentiodynamic (PD) polarization was performed at -0.25 V_{OCP} to 0.4

V_{OCP} with a 20 mV/s scanning rate. Linear fitting was performed on the Tafel plots over -0.25 V_{OCP} to 0 V_{OCP}, and over 0 V_{OCP} to 0.25 V_{OCP}, the corrosion current density was then extracted from the crossing point. Electrochemical impedance spectroscopy (EIS) was conducted at OCP with ± 10 mV stimulus potential over the frequency range of 10 kHz to 1 Hz. A programmable 3D motor with nanometer precision controlled the positioning of the micropipette to scan a grid-matrix that is superimposed on EBSD- and optical microscope mapped areas. This produced hundreds of location-specific corrosion datasets within one scan, and allowed correlation of measured properties (e.g., corrosion rate, corrosion potential, and passive film thickness, etc.). A conductive carbon-fiber cloth was used to cover the whole SECCM apparatus as a Faraday cage. A Petri dish filled with cotton saturated with LiCl solution was placed next to the scanned sample to ensure a high relative humidity and prevent microdroplets from drying. All experiments were performed at room temperature (23 ± 2°C) using reagent grade chemicals. All solutions were prepared using deionized (DI) water (>18 MΩ-cm^2).

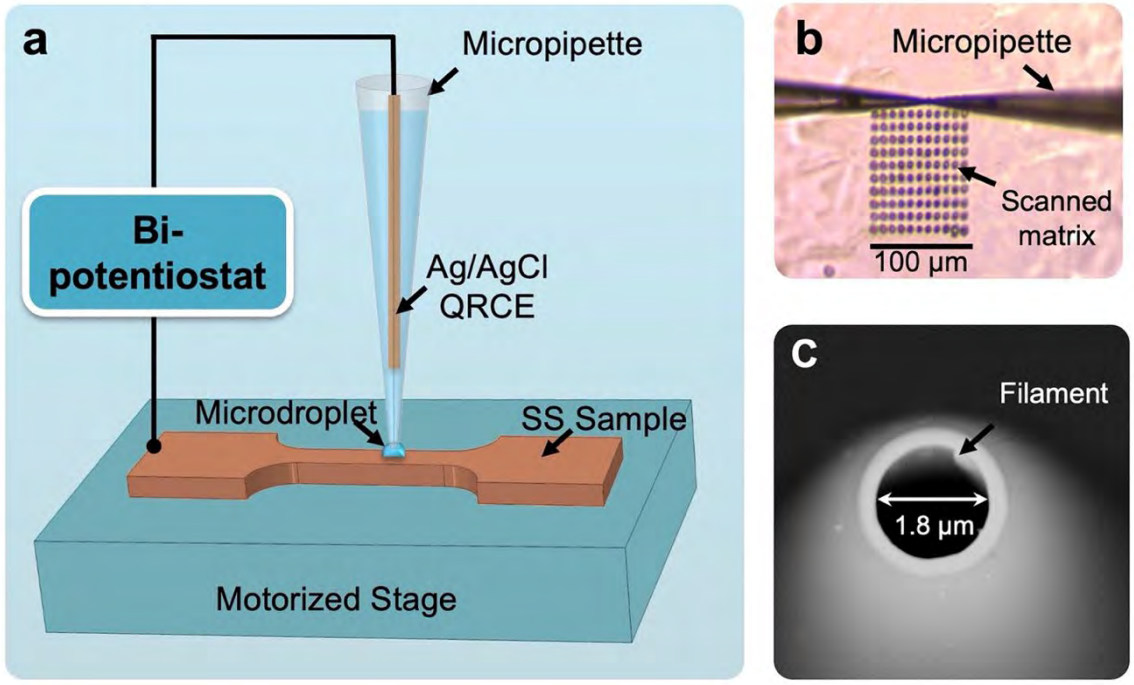

Figure 2 (a) A schematic of the scanning electrochemical cell microscopy (SECCM) setup. (b) An optical image showing the matrix of microdroplets during a scan in progress. (c) A scanning electron microscopy (SEM) image of the micropipette (filamented borosilicate) used in this study.

2.5 Surface imaging

Topographical and polarized light images were acquired by a Vertical Scanning Interferometer (VSI, Zygo, NewView 7000). A 100× Mirau objectives (lateral resolution 84 nm) were used to measure surface height over the SECCM scanned areas ranging from 80 µm × 80 µm to 1 mm × 1 mm. The resolution in the z-direction is in the order of ±2 nm based on analysis of a NIST traceable step-height standard. The Gwyddion (ver. 2.55)[22] software was used to analyze the topographical and polarized light images acquired by VSI. The SECCM scanned area were characterized immediately after each experiment to measure microdroplet sizes, and all current density and impedance were normalized by the surface area covered by microdroplets. In this study, the microdroplets are of diameters between 3 to 10 µm, rendering size measurement errors of less than 3%.

3. Results and discussion

3.1 Corrosion activity of dislocation channels

To clearly unentangle irradiation-assisted SCC (namely, IASCC), first, we exploited the surface electrochemical reactivities solely induced by irradiation. The results have been shown in previous reports. In short, an annealed 304L steel was partially irradiated to 1.1 dpa. Although the irradiation did not cause any apparent surface alternations, the irradiated area was clearly revealed by the impedance ($|Z|_{1Hz}$) map characterized by low charge-transfer resistances. As such, irradiation induces point defects, dislocation loops, etc.,[12] which lead to a defective passivation film and enhanced corrosion activity.

When the irradiated sample is further subjected to mechanical deformation, a small strain (1%) can readily cause severe dislocation channeling in the irradiated lattice (see **Figure 3c**)[23–25]. The dislocation channels (DCs) are signified by the 20-to-150 nm slip steps found on the sample surface. Evident corrosion susceptibilities of the DCs are revealed by the scanning AC-impedance measurements conducted via constant frequency and frequency sweeps (see **Figure 3d** and **3e**). Note that, an irradiation of 1.1 dpa alone can cause a 40% reduction in steel's oxidation resistance ($|Z|_{1Hz}$ from 3.7 ± 0.6 kΩ-cm^2 to 2.1 ± 0.5 kΩ-cm^2), and the resistance is further reduced to 1.2 ± 0.2 kΩ-cm^2 at DCs. Such significant reduction in charge-transfer resistance will result in fast corrosion of the surface steps, and has been confirmed by studies in simulated reactor environments[23,26]. It is indicated that the high corrosion/oxidation tendency of DCs is attributed to the following: 1) the highly distorted lattice which stores elastic energy at defects such as dislocation networks, thereby elevating the chemical potential and reactivity of the alloying atoms.[16,17] 2) DC formation leads to the formation of abrupt surface steps, which mechanically disrupt the original oxide film and expose the metal atoms directly to the corrosive environments. In fact, equivalent circuit fitting of the EIS spectra suggests the rupture of the oxide layer at the surface steps, leading to the reduced surface impedance values (see **Figure 3e** and **3f**). Moreover, the surface steps also disrupt stress flow and cause stress concentration, causing mechanical-chemical interplay (i.e., likely the root cause of IASCC initiation). Importantly, this study provides a non-destructive approach to locate and assess these detrimental features induced by irradiation and/or deformation.

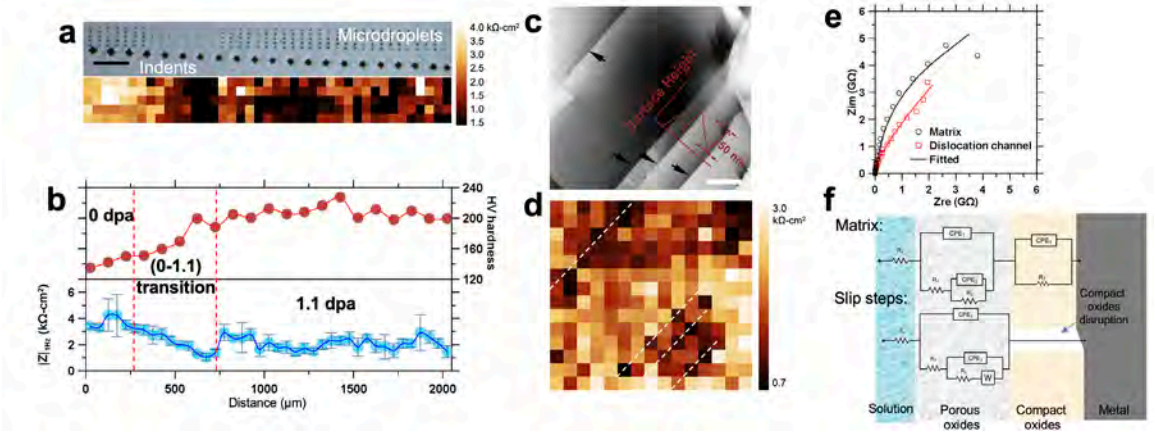

Figure 3 Scanning probe impedance analysis: constant frequency mapping of irradiated 304L. **(a)** An optical image showing matrices of microdroplets and Vickers hardness indents. From left to right, the microdroplets are 50 μm apart and the hardness indents are 100 μm apart. The scale bar is 200 μm in length. **(b)** AC-impedance at 1Hz is consistent with hardness measurements, revealing the irradiated and unirradiated regions, the transition region is highlighted by red dashed lines. The error bars of $|Z|_{1Hz}$ show the standard deviation of five repeat measurements. In an irradiated and deformed (1% strain) 304L sample, dislocation channels (DCs) are evidenced by the surface height steps. **(c)** Surface topography and **(d)** $|Z|_{1Hz}$ maps acquired from the same area indicating the DCs feature a significantly reduced corrosion

resistance. The scale bar in **(c)** is 20 μm in length, and a 20 mM LiCl + 5 % HNO_3 solution was used in all impedance scans. **(e)** Full frequency spectra (1 Hz - 1 kHz) of the irradiated matrix and a dislocation channel, the data were fitted by equivalent circuit models indicated in **(f)**. We noticed that the passive film formed on the matrix has a two-layered structure: a compact layer and a porous layer. However, only a porous layer was observed at the slip steps, indicating the disruption of compact layer during deformation.

3.2 Microstructural evidence of oxide disruptions at dislocation channels

To confirm corrosion activities identified in SECCM tests, we have employed STEM to explore microstructure of the dislocation channels and their surface oxides. Our findings are as follows: i) the presence of a 10 nm oxide layer on top of the substrate and its absence at the DC steps, which might explain the passivation degradation observed from the impedance analysis (**Figure 3**), ii) a detailed characterization of the dislocation channels (DCs) coming from different steps with a thickness around 25 nm and with the characteristic weak satellite reflections from their dislocation arrays, iii) the diffusion of Cr through the grains to form complex $FeCr_2O_4$ oxides that leaves some Cr depletion areas along GBs, iv) the determination of crystallographic orientation relationships between γ (austenite) and α (ferrite) phases and the complex $FeCr_2O_4$ oxides. In the following we provide a thorough description of the two [H^+]-irradiated stainless steel samples with 1.1 dpa dose and was deformed to 1%.

From the TEM analysis of sample#1 (**Figures 4-11**), we were able to characterize the dislocation channels (DCs) and the inner layer of around 10 nm scale made of an oxide as verified later with the EDS analysis. We confirmed that the oxide layer was missing at the steps, which might explain the passivation degradation that was observed from the impedance analysis. An average step height of 90 ± 23 nm was measured. At least two dislocation channels (DCs) parallel to the {110} and $\{13\bar{1}\}$ planes have been identified coming from different steps with a thickness around 25 nm. We found two pairs of edge dislocations on the $\{1\bar{1}1\}$ planes separated 0.6 and 1 nm, and two partials lying on the same slip plane. Weak satellite reflections parallel to the <110> slip directions were also found as an indication of regular dislocation arrays in the DCs.

TEM data of another step from the Stainless-Steel (SS) sample #2 (**Figures 12-17**), reveals a DC parallel to the (110) planes. Different layers of surface coatings (oxides and Pt) have been identified with different contrast using bright field (BF), dark field (DF) and high-angle annular dark field (HAADF) detectors under the STEM mode. STEM images confirmed the presence of an oxide layer around 10 nm found between the Pt deposited layers and the SS substrate. EDS maps have confirmed the composition of each layer. In particular, a higher concentration of O and Fe have been found at the oxide layer, suggesting an Fe-rich oxide. This has been confirmed by the spot analysis. STEM images of the DC steps revealed the thinning of the O-rich layer on top of the substrate conforming the oxide layer, this is consistent with the findings from sample #1.

In summary, the TEM-STEM results provide strong evidences that confirms the passive film disruption resulted in elevated corrosion activity as characterized by SECCM (**Figure 3**).

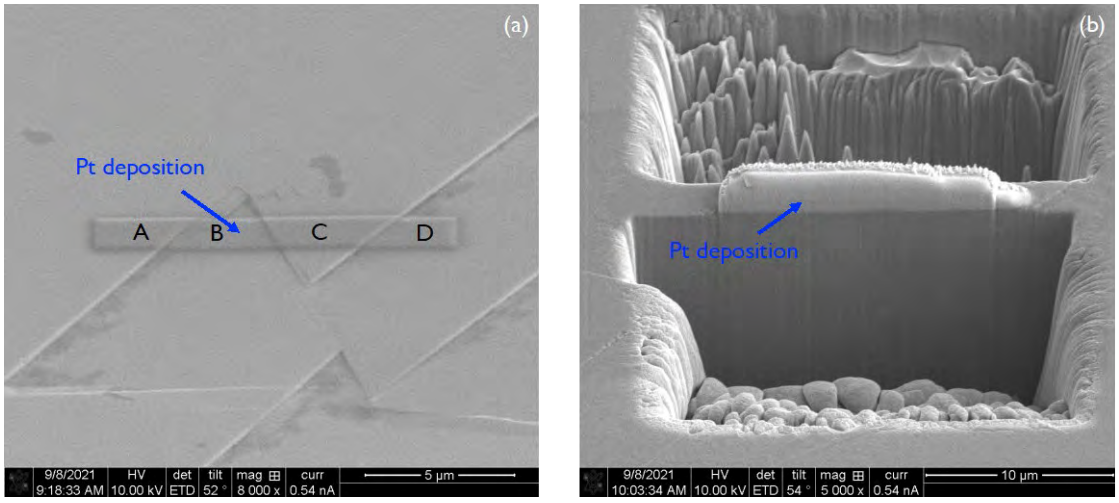

Figure 4 TEM sample preparation by FIB. (a) The irradiated 304L Stainless Steel (SS) sample #1 covered with a Pt layer for surface protection. Regions of study are named as A, B, C and D. (b) Milling process during the cross-sectional thin slide preparation.

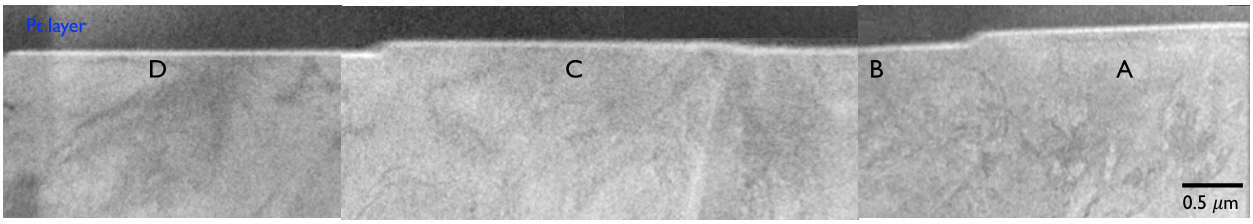

Figure 5 TEM images showing the top surface steps (the brightest layer) from the irradiated process. The measured steps height is around 90 ± 23 nm

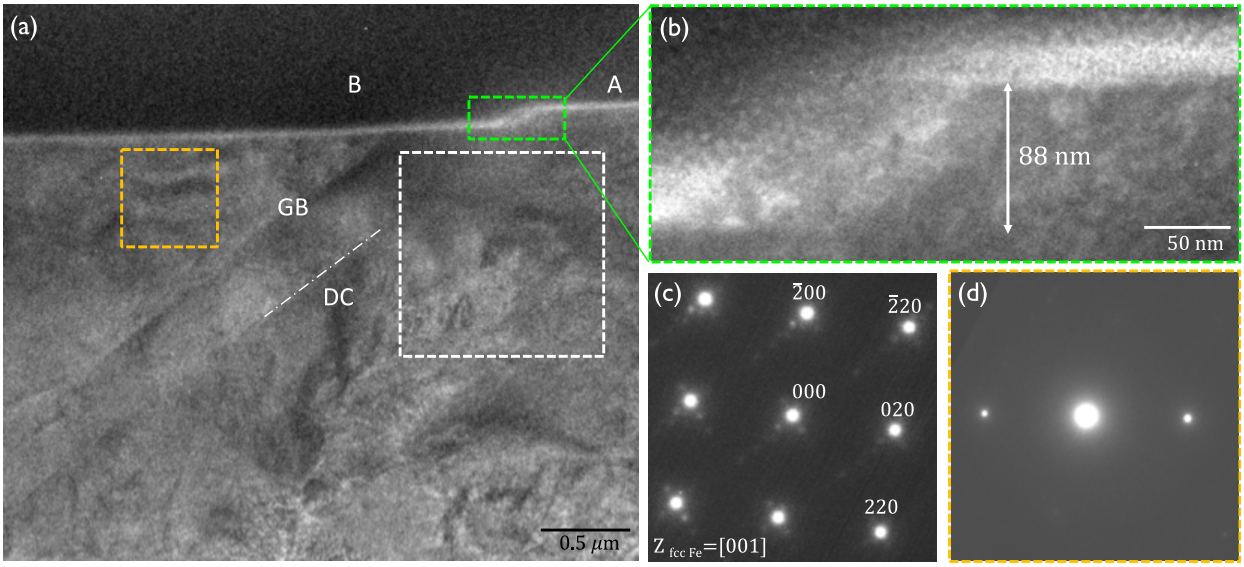

Figure 6 (a) TEM image showing a dislocation channel (DC) coming from the step between A and B regions and a grain boundary (GB). This step with a height of 88 nm can be better seen at higher magnification in (b). DC results to be parallel to the {220} planes as confirmed by the selected area electron diffraction (SAED) pattern of a fcc austenitic grain oriented to the [001] zone axis [1] (c). Note

the weak satellite reflections parallel to the <110> slip directions that might be due to regular dislocation arrays in the DC. (d) SAED pattern from the yellow square region of the neighboring grain oriented to a different zone axis, which verifies the presence of the GB.

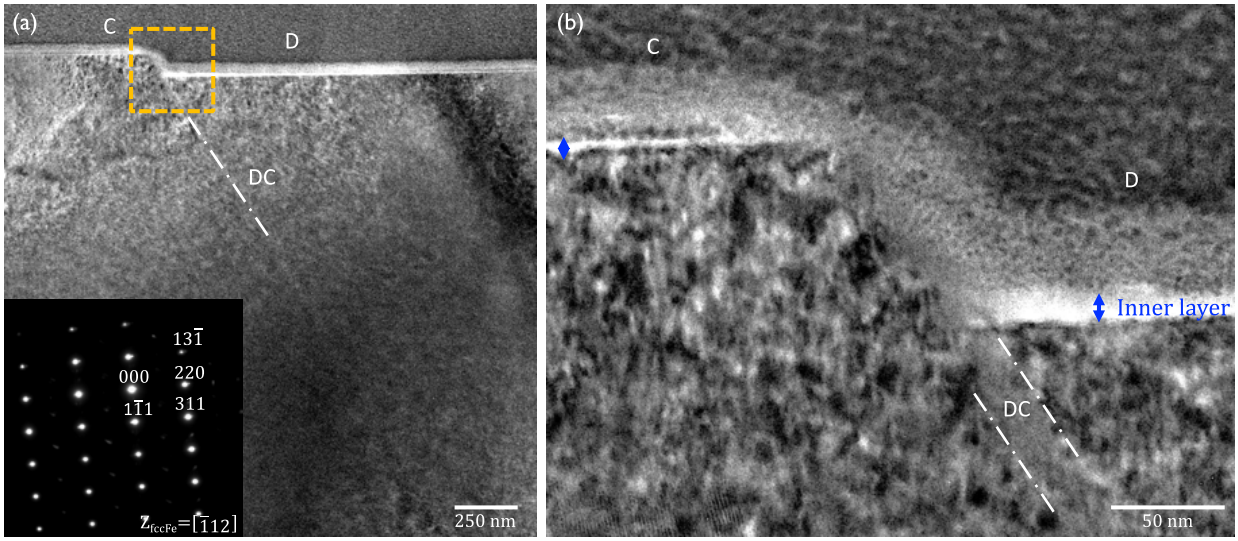

Figure 7 (a) TEM image of the C/D step where the grain behind has been oriented to the $[\bar{1}12]$ zone axis as reveals its SAED pattern (inset) [1]. DC is parallel to $\{13\bar{1}\}$ planes. (b) A close-up view of the region highlighted in (a) showing a DC of 25 nm thick. From the different contrast of the top surface layer, we identify an inner layer of around 10 nm thick. It is evident that this thin inner layer is missing at the step.

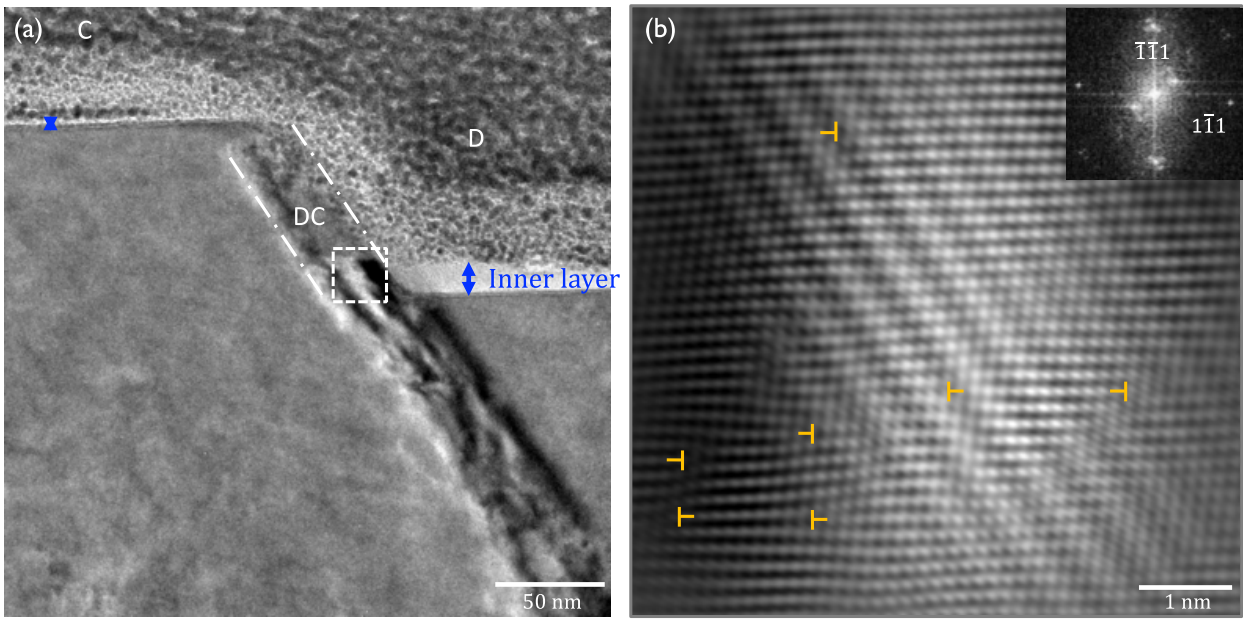

Figure 8 (a) TEM image of the same C/D step but tilted away from the $[\bar{1}12]$ zone axis. (b) Atomic resolution TEM image from the enclosed region within the DC exhibiting edge dislocations (highlighted in yellow) on the $\{1\bar{1}1\}$ planes as confirmed by its FFT. Among those dislocations, we can identify two pairs of edge dislocations separated 0.6 and 1 nm, and two partials lying on the same slip plane.

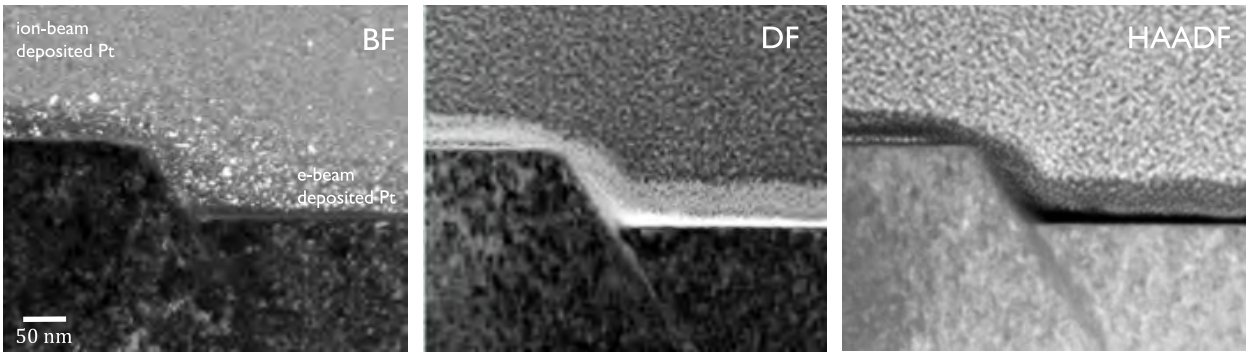

Figure 9 STEM images of the C/D step. Bright field (BF), dark field (DF) and high-angle annular dark field (HAADF) STEM images at higher magnification showing different contrast between layers because of differences in composition.

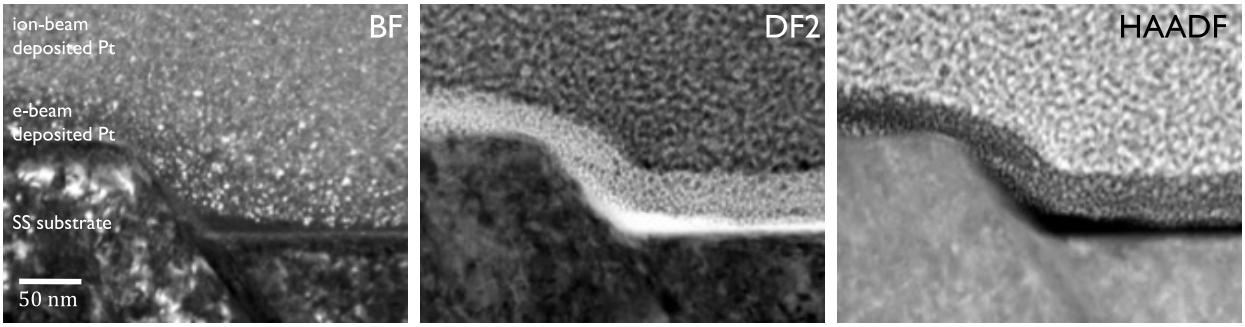

Figure 10 22◦ tilted-view STEM images of the C/D step at higher magnification. The interface between the e-beam deposited Pt layer and the SS substrate (black in color for instance in the HAADF image) indicate a gap between the deposited Pt layer and the substrate.

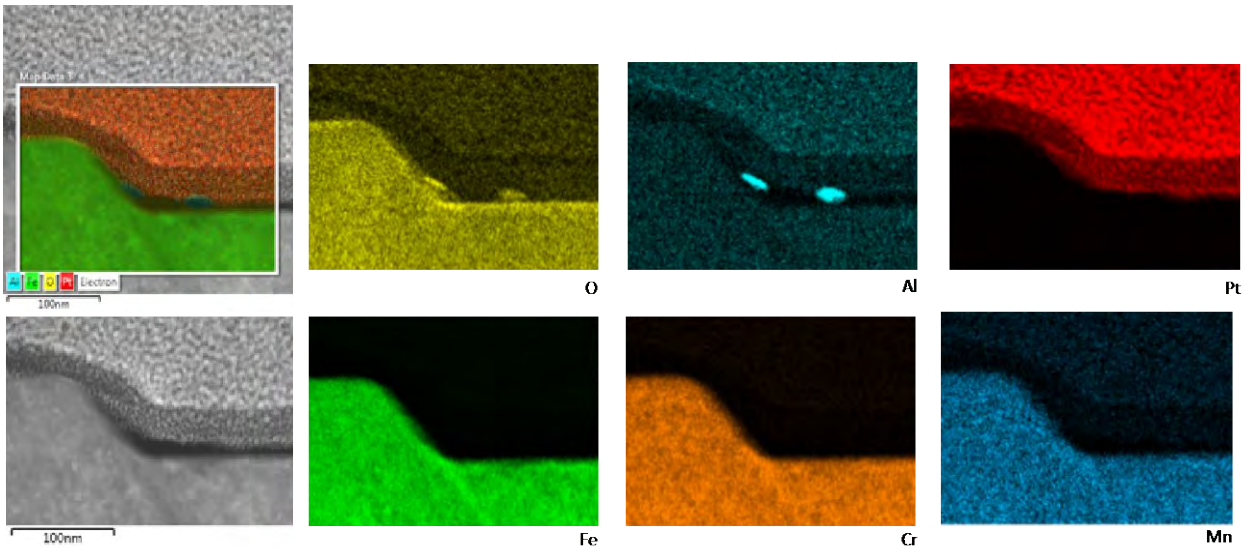

Figure 11 EDS mapping of the step at 22◦ of alpha tilt angle. O- EDX map reveals a thin oxide layer around 8 nm thick on top of the SS substrate. Comparing the Fe and Cr-maps, this oxide layer seems to be rich in Fe. The interface between the e-beam deposited Pt layer and the SS substrate is still black conforming the gap between the deposited Pt layer and the substrate. Additionally, two small particles

rich of O and Al (probably some remaining Al_2O_3 powders from the polishing process) have been identified inside of the gap.

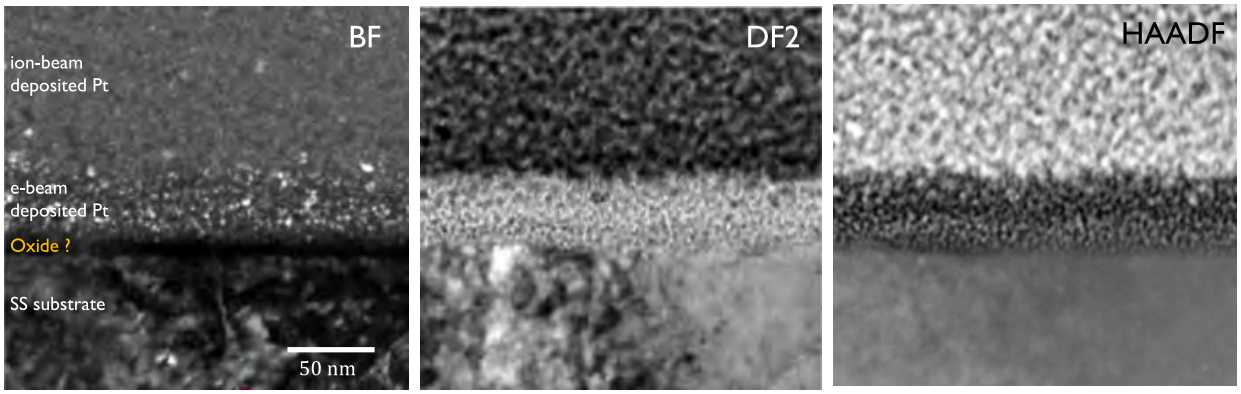

Figure 12 22° tilted-view STEM images out of the step region at higher magnification. No gap is visible at the interface between the e-beam deposited Pt layer and the SS substrate

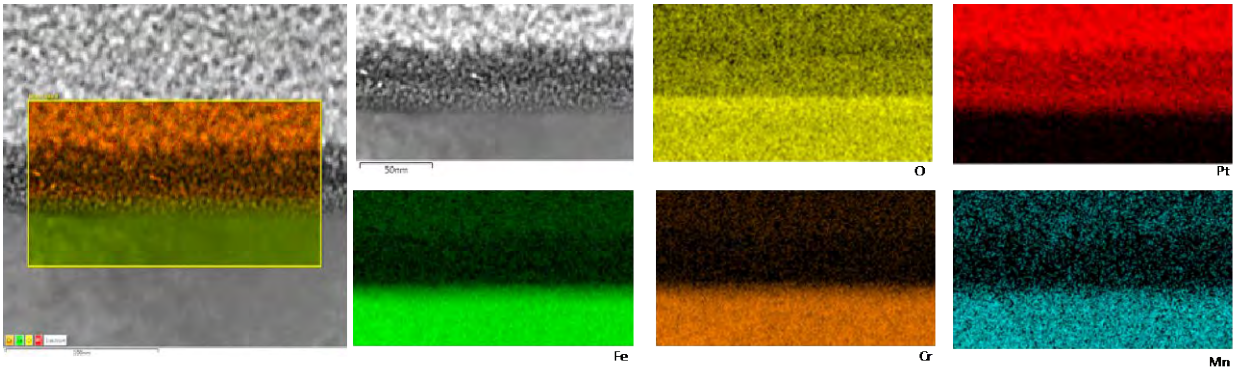

Figure 13 EDS mapping out of the step. An O-rich layer is identified on the top of the SS-substrate

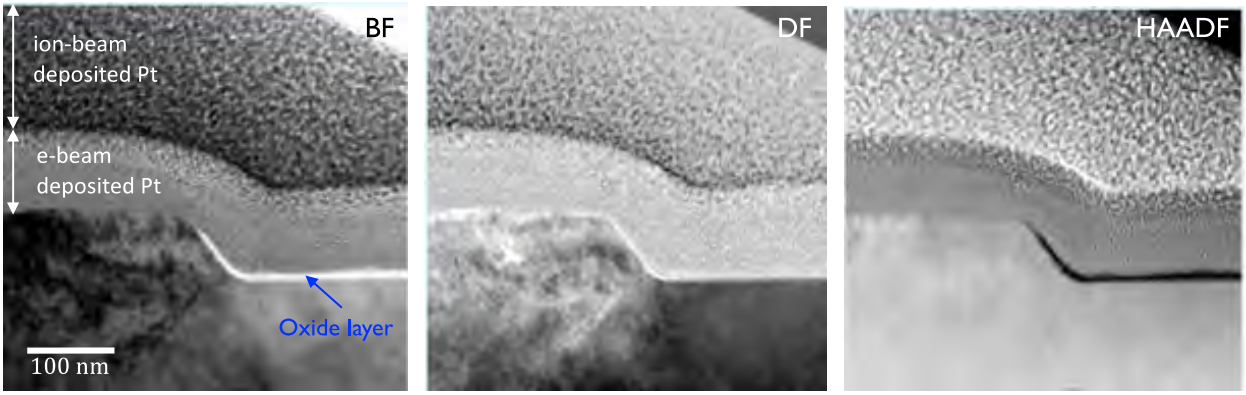

Figure 14 STEM images of the SS sample #2 step region at higher magnification. Different layers can be seen with different contrast using bright field (BF), dark field (DF) and high-angle annular dark field (HAADF) detectors. An oxide layer might be at the interface between the e-beam deposited Pt layer and the SS substrate.

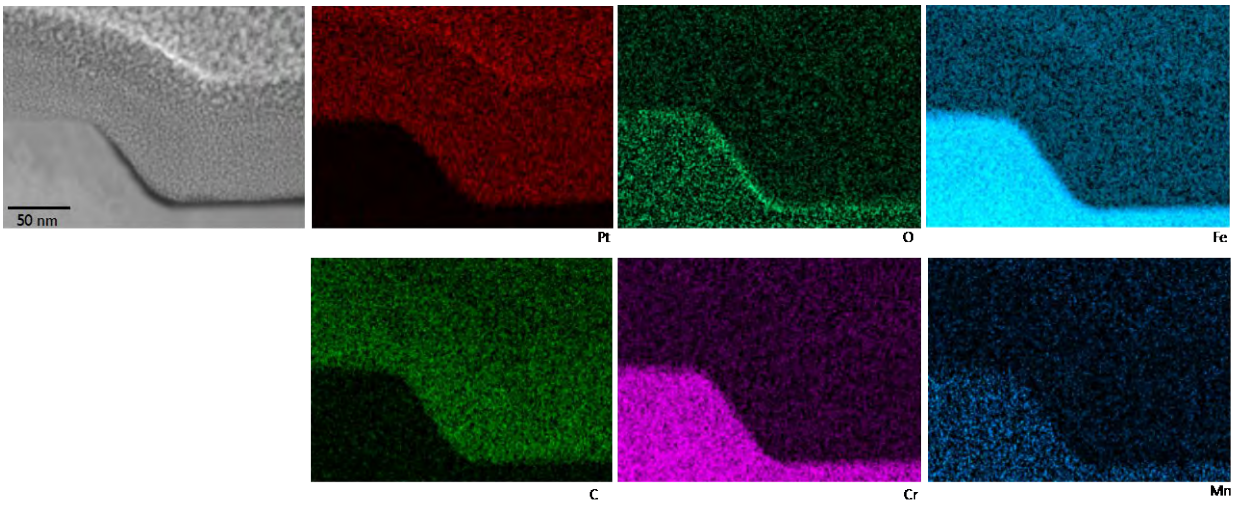

Figure 15 EDS mapping of the step showing higher concentration of O between the Pt layers and the SS substrate

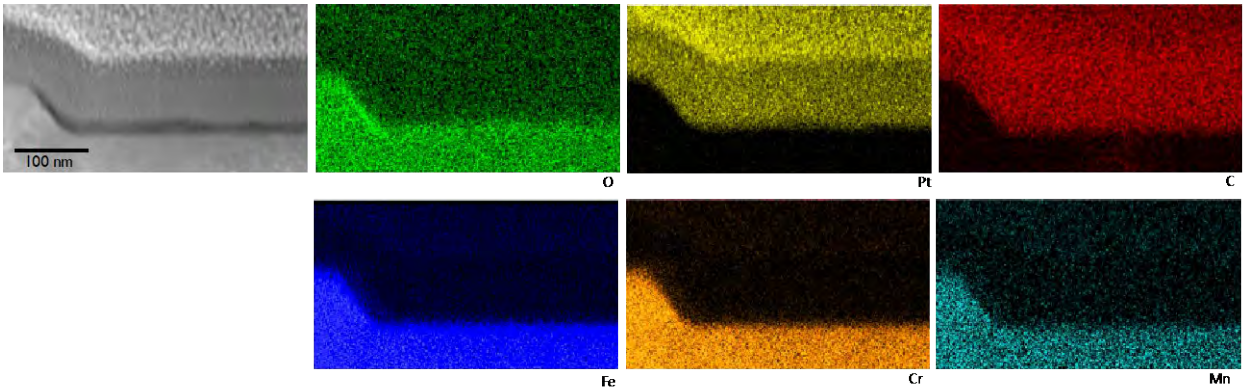

Figure 16 Additional EDS data confirming the higher concentration of O at the interface, which suggests the presence of an Fe-rich oxide layer.

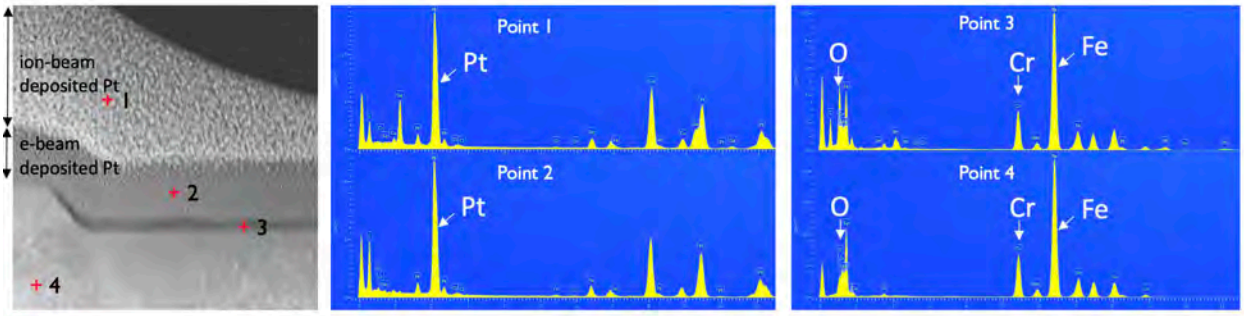

Figure 17 EDS spot analysis form the step. Spectra from points 1 and 2 confirm the two Pt deposited layers. Note the Ga peak from point 1 characteristic of the ion beam Pt deposition. The O peak from point 3 verifies the presence of the oxide layer. Comparing the spectra from point 3 (oxide layer) and 4 (substrate), the ratio between the maximum intensity peaks for Fe and Cr is the same for point 3 and point 4, indicating the similar composition of Fe and Cr in the bulk and in the oxide layer. However, the K_α/L_α

Fe intensity ratio is higher at point 3 (2.2) than that for point 4 (1.92), which may indicate the oxide layer is slightly enriched by Fe.

3.3 Grain boundary microstructural evolution of a [Fe^{++}]-irradiated stainless steel

In addition to dislocation channels, interesting findings were obtained from microstructural characterizations of grain boundaries. A cross-sectional TEM sample from a [Fe++]-irradiated stainless steel (5 dpa) was prepared by FIB to identify any possible Cr depletion and Ni segregation at the grain boundary. The presence of these $FeCr_2O_4$ oxides proves once again that Cr diffuses through the grains and grain boundaries to form those oxides leaving some Cr depletion areas along GBs, and the detailed description are listed as **Figures 18-29**. Distinguished from H-irradiation at 1 dpa, 5 dpa Fe-irradiation produces a thin band (~100nm) of α-phase (bcc) at the grain boundary. The α-phase is identified as a Fe- and Ni-enriched Fe(Ni) solid solution. $FeCr_2O_4$ precipitates were located at the interface between γ-and α-phases, suggesting the Cr-depletion at the grain boundary. However, the extend of Cr depletion is extremely small, and is confined at a very small region (5-10 nm, see **Figures 21 and 28**). Nevertheless, Cr-depleted GBs are expected to have higher corrosion reactivity. However, as indicated in our previous reports, SECCM was not able to resolve the corrosion rate/resistance differences between the grain boundary (GB) and the grain interior (GI).

Figure 18 SEM characterization of the SS sample#3 tensile specimen. Only a few grains are visible within the gauge length (highlighted by green arrows).

In order to determine the grain size and to identify different phases in the sample, high-resolution SEM images were obtained using backscattered electrons (BSE). By way of example, see Fig. 19

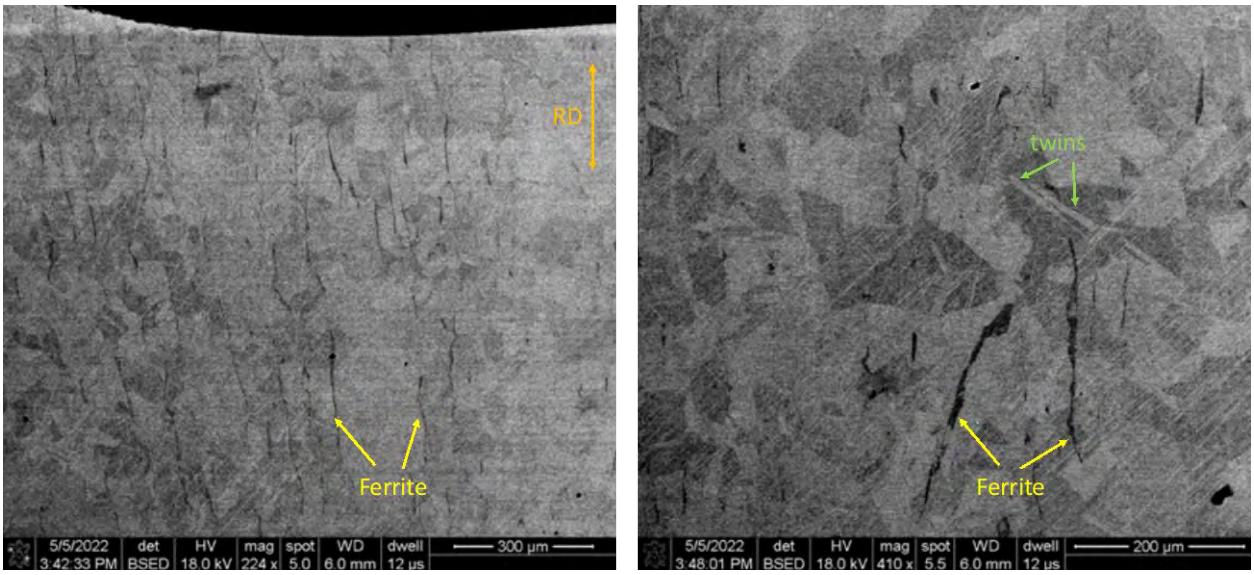

Figure 19 BSE-SEM images showing austenitic grains with an average grain size of 57 ± 27 μm. Many twins can be observed within the austenitic grains. Also, the retained ferrite phase can be seen in dark contrast and elongated along the same direction, which might be an indication of the rolling direction (RD).

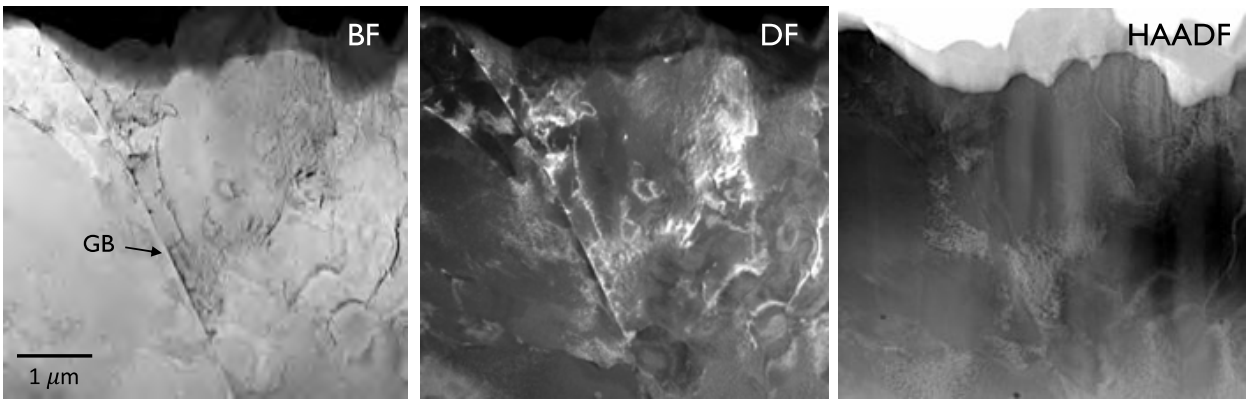

Figure 20 STEM analysis of the cross-sectional TEM sample. Bright field (BF), dark field (DF) and high-angle annular dark field (HAADF) STEM images of the specimen showing the GB at the center under different contrast.

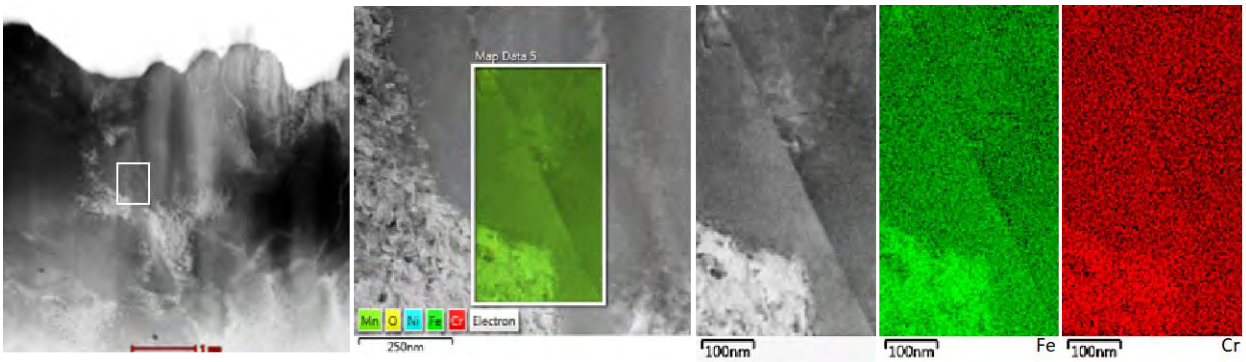

Figure 21 EDS mappings of the enclosed region from the grain boundary. The spatial distribution of Fe and Cr seems not to be uniform along the GB. The EDS mapping reveals GB regions where the Cr content is higher while the Fe content is lower and vice versa. This might be an indication of Cr depletion areas along the GB

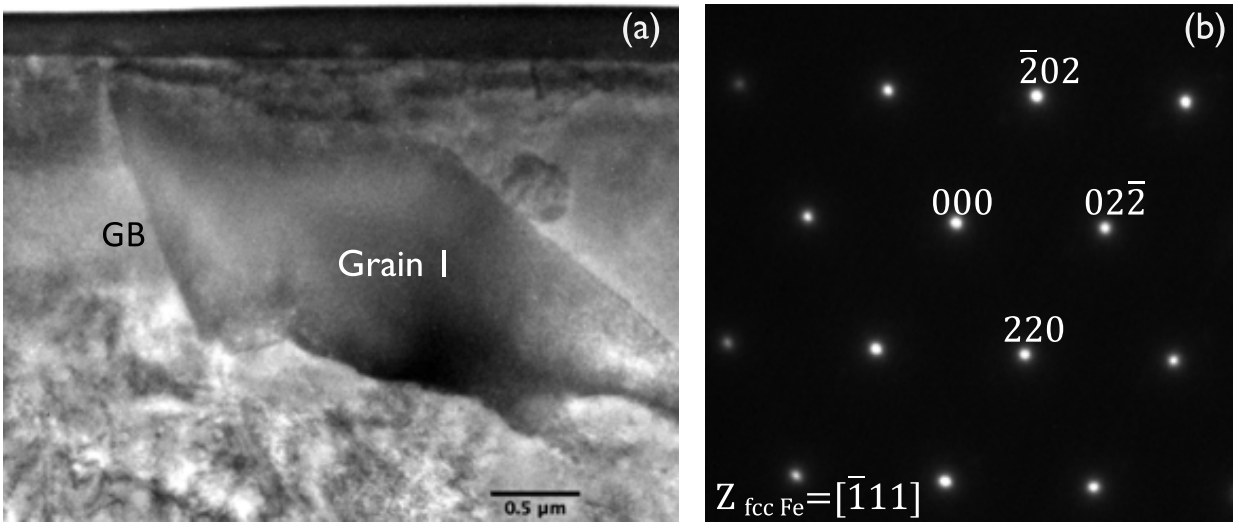

Figure 22 (a) TEM image of a grain to the right of the GB (Grain 1) oriented to the [$\bar{1}11$] zone axis as reveals in selected area electron diffraction (SAED) pattern in (b).

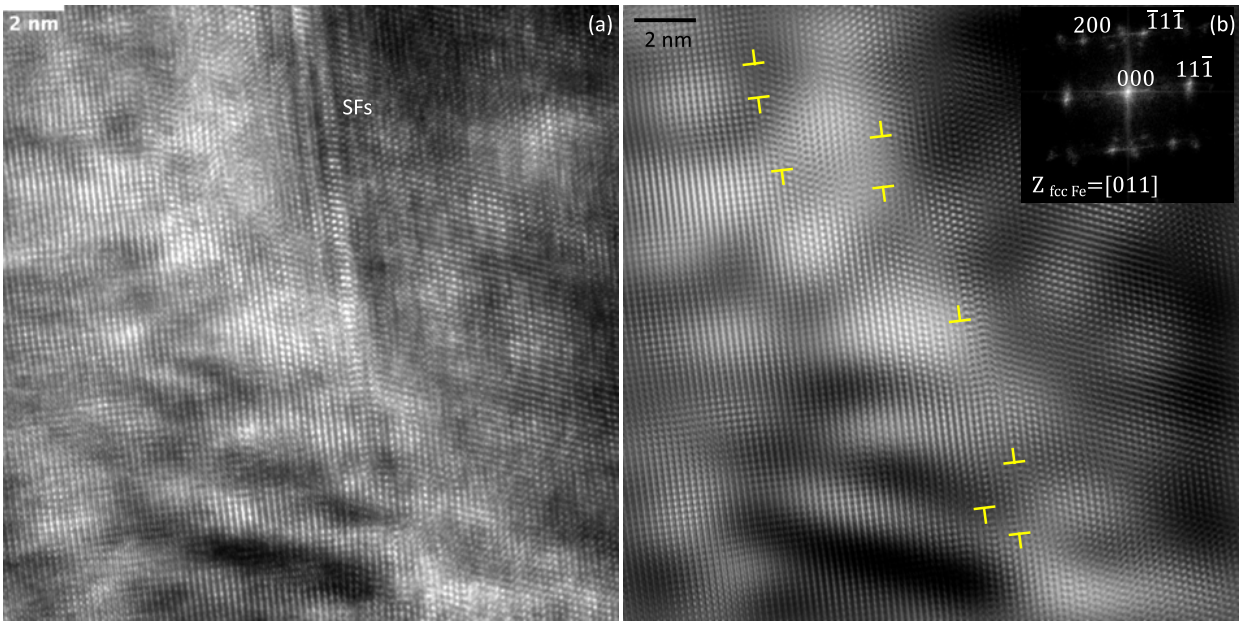

Figure 23 (a) Atomic resolution TEM images of another grain. Defects such as stacking faults (SFs) are also visible. (b) Inverse FFT TEM image showing SFs on the $\{11\bar{1}\}$ planes bounded by partial dislocations highlighted in yellow as confirmed by its FFT (inset).

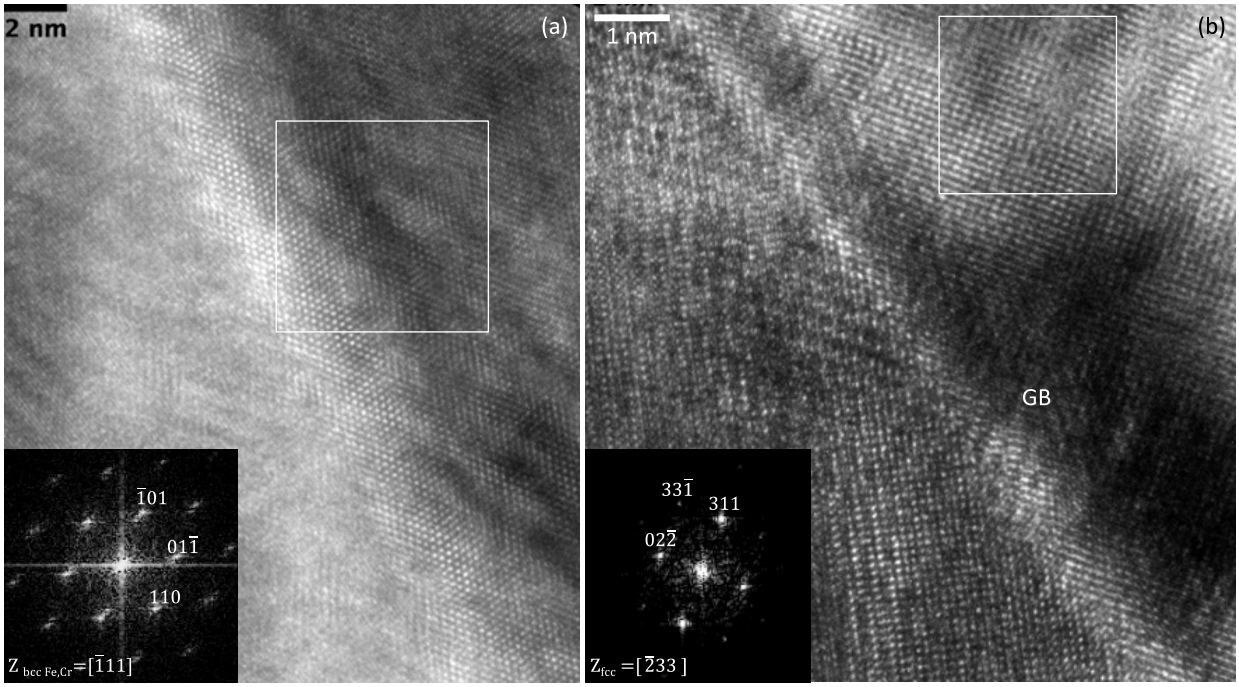

Figure 24 Atomic resolution TEM images conforming the presence of different phases along the GB. FFT from the region enclosed by the white square confirms the $[\bar{1}11]$ zone axis of a ferritic phase with a bcc structure in (a), and a complex Cr-Fe oxide ($FeCr_2O_4$) oriented to the $[\bar{2}33]$ zone axis in (b) [3].

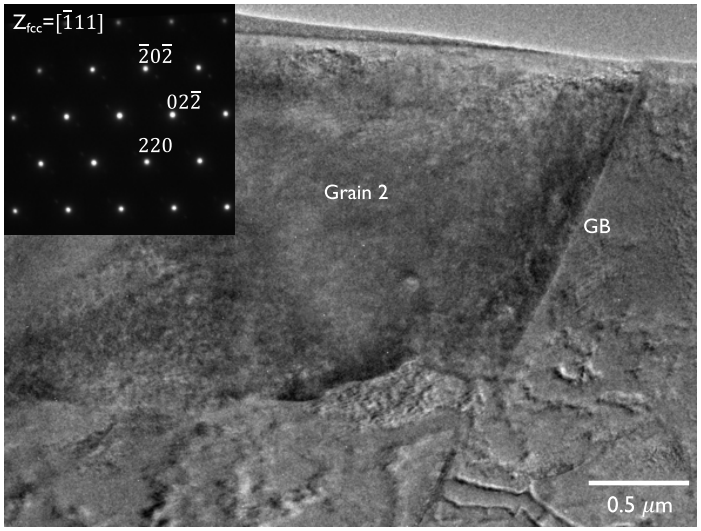

Figure 25 TEM image of the GB region after tilting the grain to the left (Grain 2) to the perfect $[\bar{1}11]$ zone axis as shown by its SAED pattern (inset).

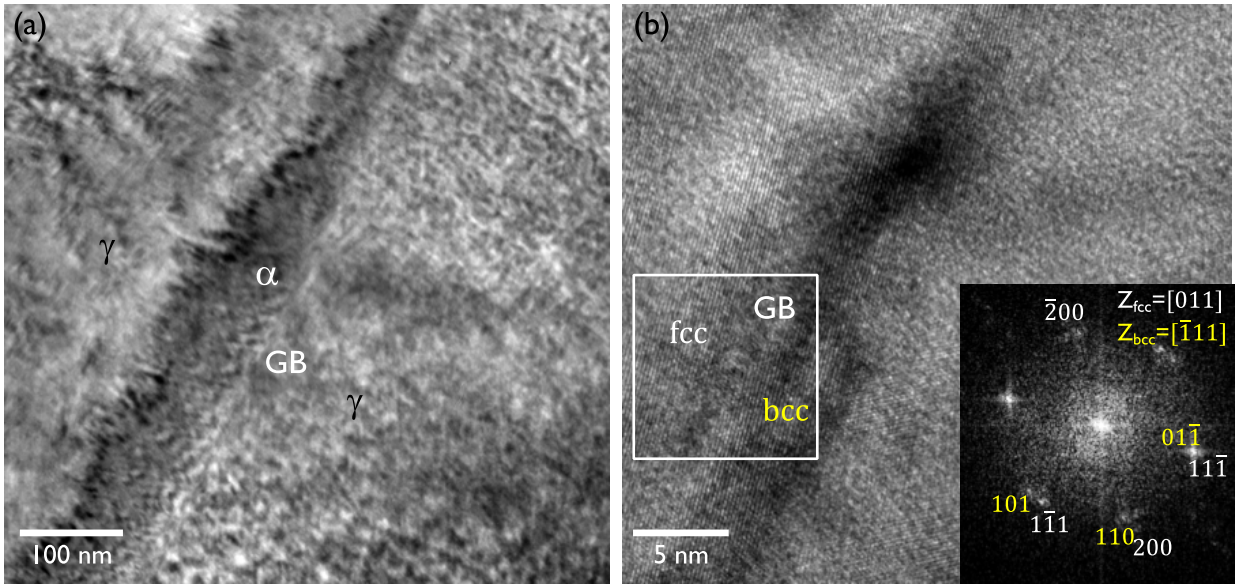

Figure 26 (a) TEM images displaying the α ferrite morphology along the GB surrounded by γ austenitic grains. (b) HRTEM image enclosing the two phases. Indexed FFT of the squared region confirms the presence of bcc α phase (highlighted in yellow) along the GB. The bcc phase oriented to the $[\bar{1}11]$ zone axis is parallel to the [011] zone axis of the γ phase. Under this orientation, the following relationship is stablished between both phases: $(01\bar{1})_{bcc}$ // $(11\bar{1})_{fcc}$.

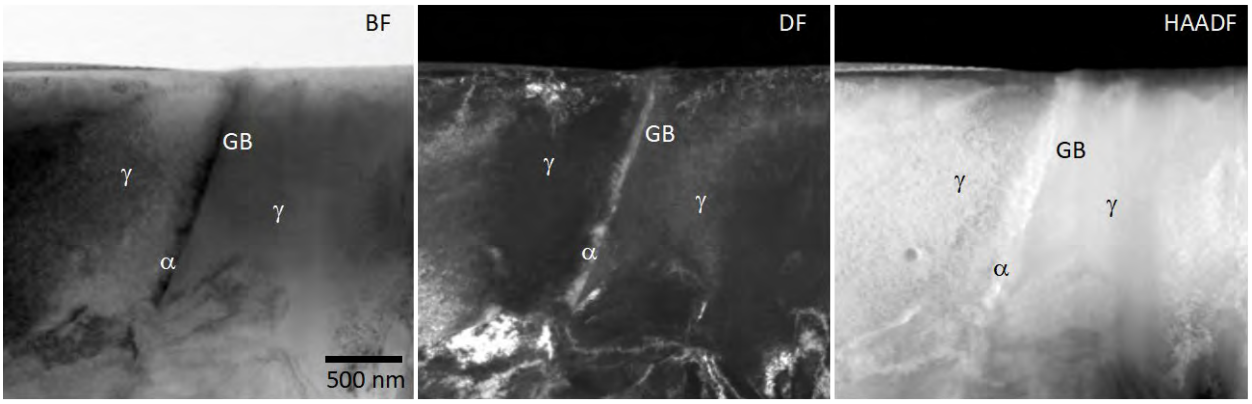

Figure 27 STEM analysis of the grain boundary (GB) and the phases surrounding. Bright field (BF), dark field (DF) and high-angle annular dark field (HAADF) STEM images showing the GB, the γ grains and the α phase in different contrast

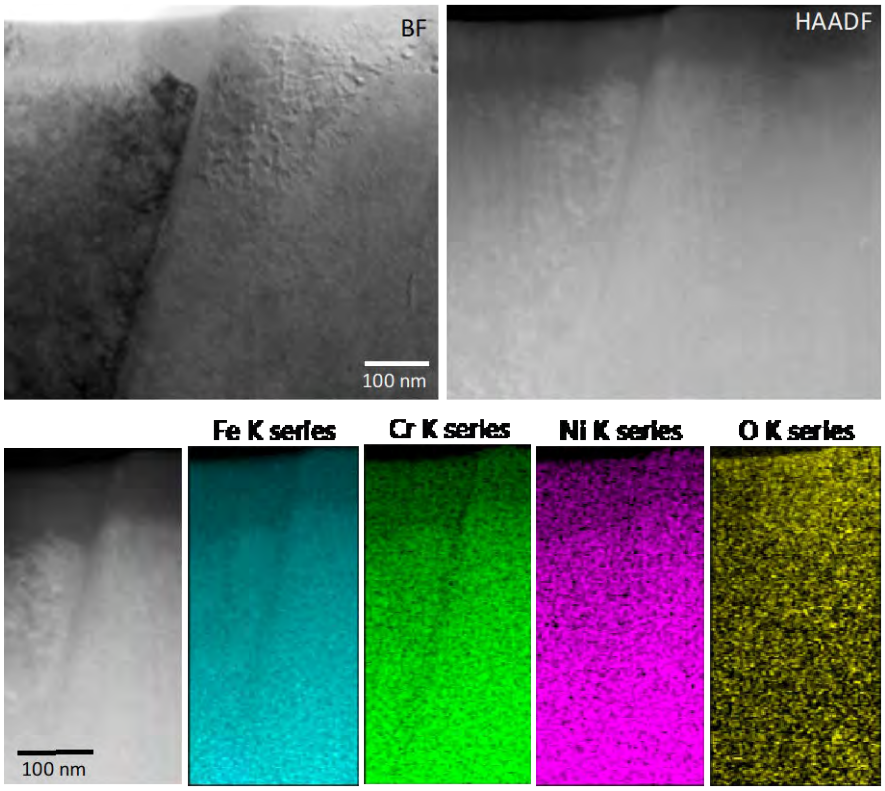

Figure 28 EDS mapping of the STEM image conforming the Cr depletion at the top part of the GB as we observed before. Fe content seems to be lower as well.

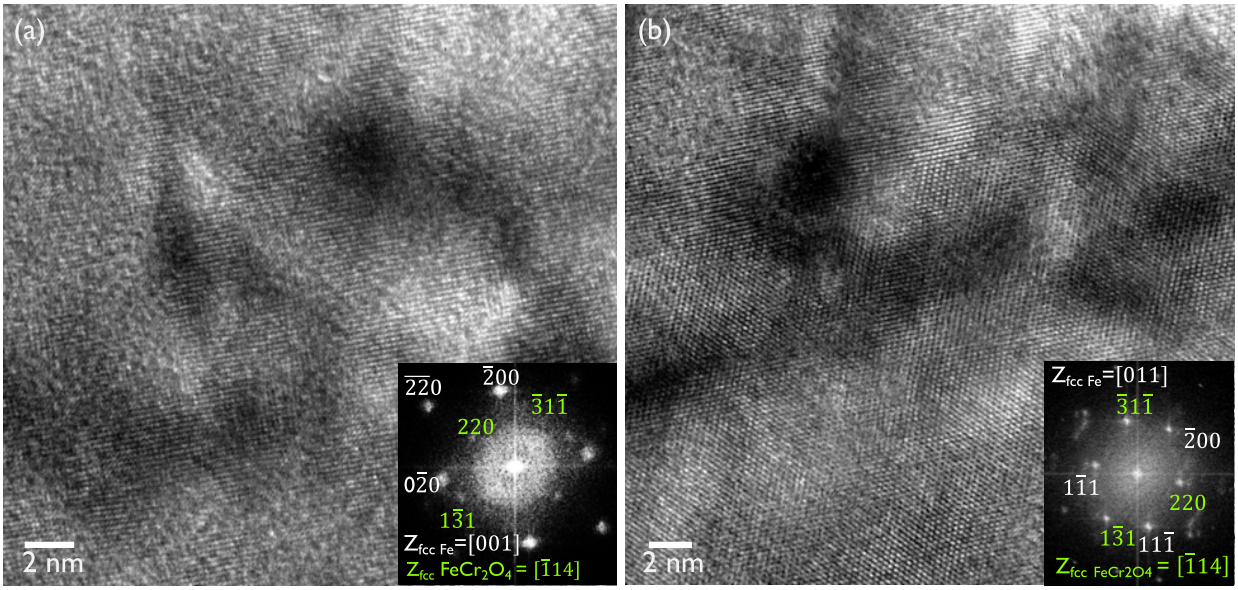

Figure 29 Atomic resolution TEM images confirming the presence of complex oxides such as $FeCr_2O_4$ within the austenitic grains. (a) Indexed FFT of the image (inset) confirms the presence of $FeCr_2O_4$ oxide (highlighted in green) oriented to the $[\bar{1}14]$ zone axis [3] that is parallel to the [001] zone axis of the austenitic grain. Under this orientation, the following relationship is stablished between both phases: $(220)_{\gamma Fe}$ // $(220)_{FeCr2O4}$. (b) Indexed FFT of the image (inset) confirms the presence of $FeCr_2O_4$ oxide (highlighted in green) oriented to the $[\bar{1}14]$ zone axis that is parallel to the [011] zone axis of a different austenitic grain. Under this orientation, the following relationship is stablished between both phases: $(11\bar{1})_{\gamma Fe}$ // $(\bar{3}1\bar{1})_{FeCr2O4}$.

3.4 Corrosion activity of irradiated grain boundaries

The insensitive corrosion activity at GBs is likely due to the Cr-depletion is not severe enough to induce passivity break down. To confirm, we have used the same approach to examine an austenitic (316L) stainless steel sample that was irradiated to 2 dpa by 5 MeV Ni++ ions. Consistently as shown in **Figure 30** and **Table 2**, SECCM can only reveal enhanced corrosion reactivity at GBs via statistical analyses. And no significant difference in corrosion activity was observed between grain interiors (GI) and grain boundaries (GB). This may be resulted from 1) not enough dpa or Cr depletion, and 2) GB characteristics, and not all GBs were subjected to irradiation-induced Cr depletion.

We consequently examined a 316L SS with much greater irradiation dose: another sample partially irradiated to 80 dpa with Ni++ ions. Vertical scanning interferometry was able to resolve the irradiation induced swelling. The sample was partially covered by a TEM grid mesh before irradiation, rendering irradiated regions in contrast to the unirradiated regions (see **Figure 31**). By measuring surface elevation, we have determined radiation induced volumetric expansion (RIVE) of the samples irradiated to 2 and 80 dpa as 0.7% and 2.5 %, respectively. Herein, RIVE measured by VSI is consistent with the literature radiation induced swelling (of other ions) value. And the partial irradiation coupled with VSI can be adapted as a high-throughput method to determine RIVE and screen swelling resistance of alloys, avoiding TEM study for swelling investigation.

Instead of performing SECCM, the 80 dpa sample was electrochemically etched in oxalic acid. After etching, irradiated region (IR) show significant regression as compared to non-irradiated region (NIR), suggesting a higher electrochemical reactivity of the IR (see **Figure 32**). Irradiation induced corrosion sensitivity of GBs were also characterized by VSI (**Figure 33**). Generally, GBs with higher corrosion activity have higher surface retreat that can be revealed by VSI. As shown, even up to 80 dpa, not all GBs

are subjected to irradiation induced corrosion sensitivity, and GB characteristics play a determining role. This might explain why SECCM can only reveal a small difference in corrosion resistance only via statistical analysis. Nevertheless, VSI coupled with electrochemical etching could be an effective tool to investigate the radiation induced swelling and screen swell-resistant alloys as LWR components.

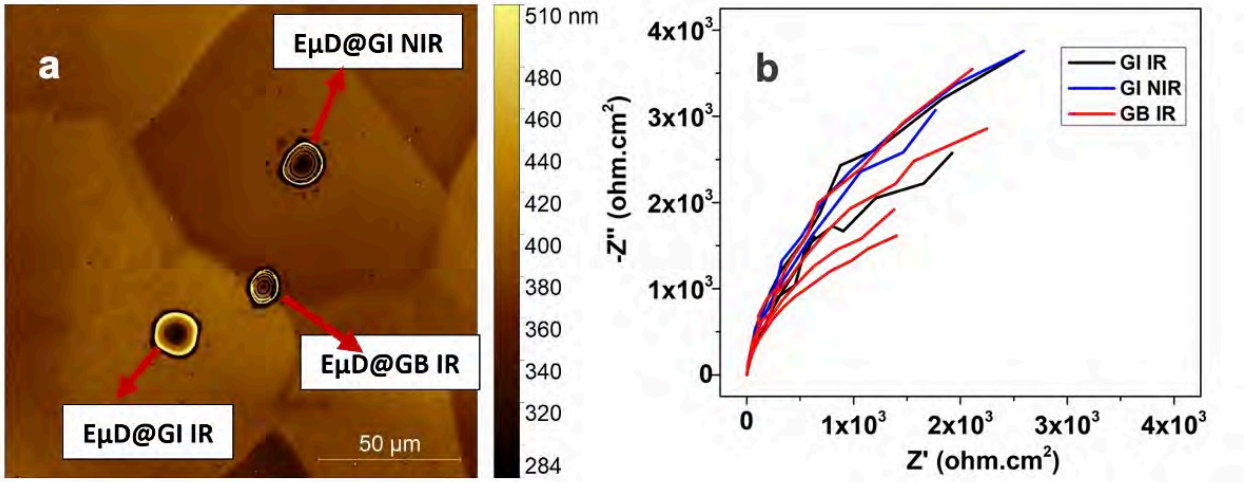

Figure 30 (a) Exemplary SECCM point analysis on grain boundaries (GB) and grain interiors (GI) of a 5 MeV Ni++ ion irradiated (2 dpa) austenitic (316L) stainless steel. (b) Exemplary impedance spectra of

Table 2 Regressed corrosion resistances of the 2 dpa, [Ni++]-irradiated stainless steel.

Parameters/ Sample region	**Corrosion resistance (kohm.cm^2)**
Grain interior (not irradiated)	**8.7 ± 0.0**
Grain interior (irradiated)	**7.1 ± 1.1**
Grain Boundary (irradiated)	**5.7 ± 2.0**

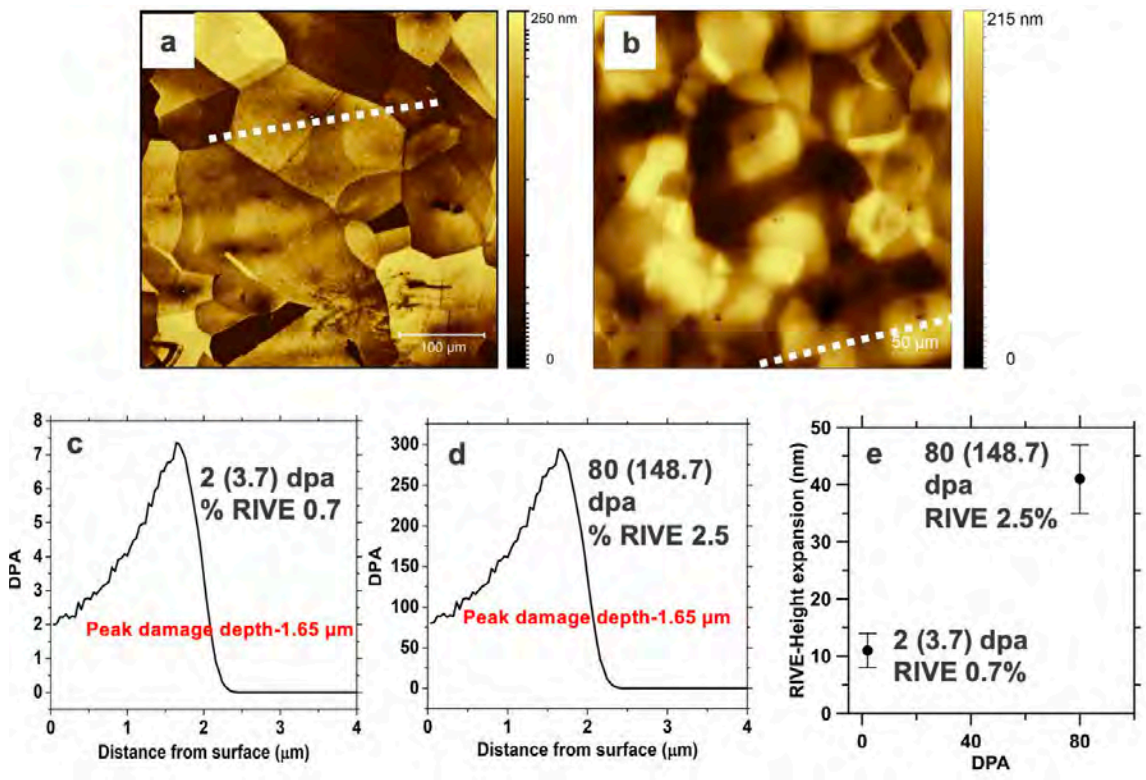

Figure 31 VSI topographical measurements of the (a) 2 dpa, and (b) 80 dpa [Ni++]-irradiated samples. (c) (d) SRIM simulation reveals the dpa distribution along the depth profile (e) RIVE determined from surface elevation measured by VSI. N.B., 2 and 80 dpa are the targeted surface damages, whereas the averaged dpa along the irradiated depth are 3.7 and 148.7 dpa, respectively.

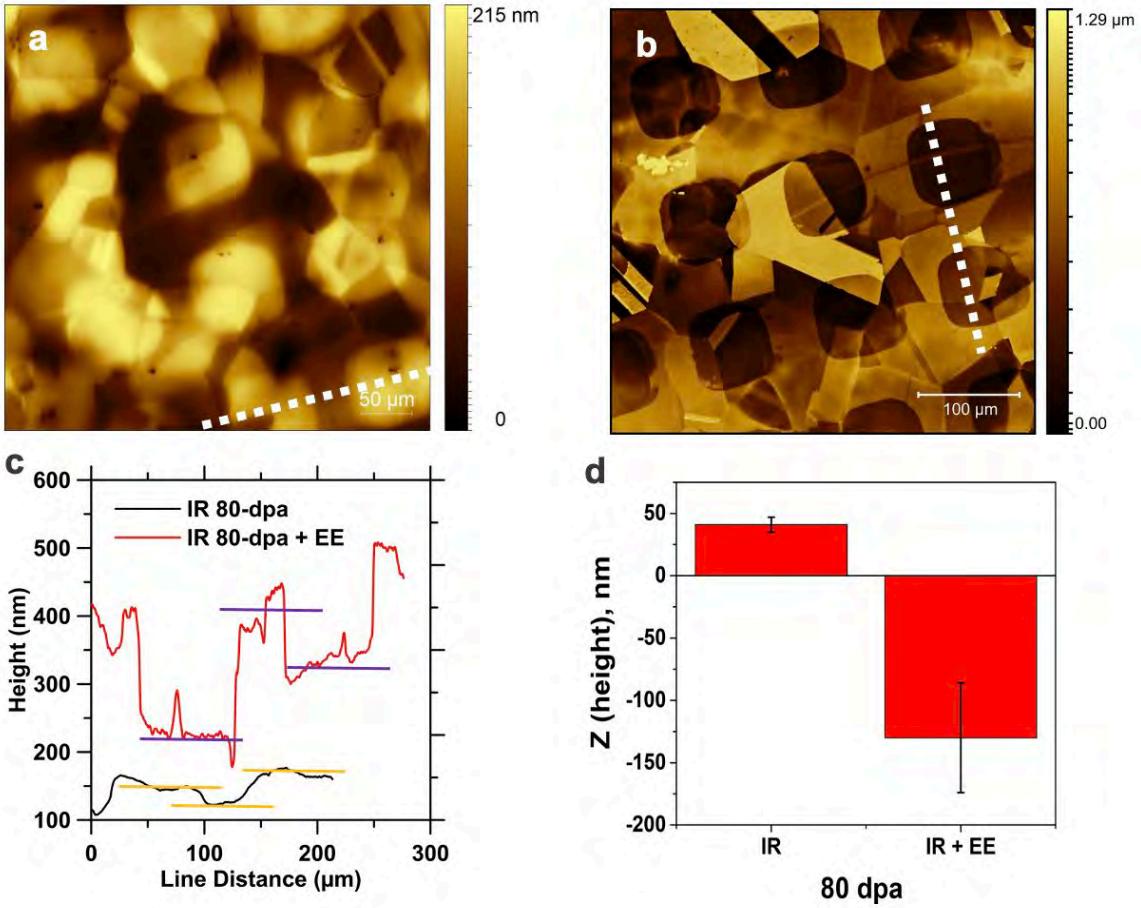

Figure 32 VSI images of the 80 dpa SS sample (a) before and (b) after the electrochemical etching. (c) (d) Surface height line profile showing the irradiated region (IR) are of the greater surface retreat after electrochemical etching (EE).

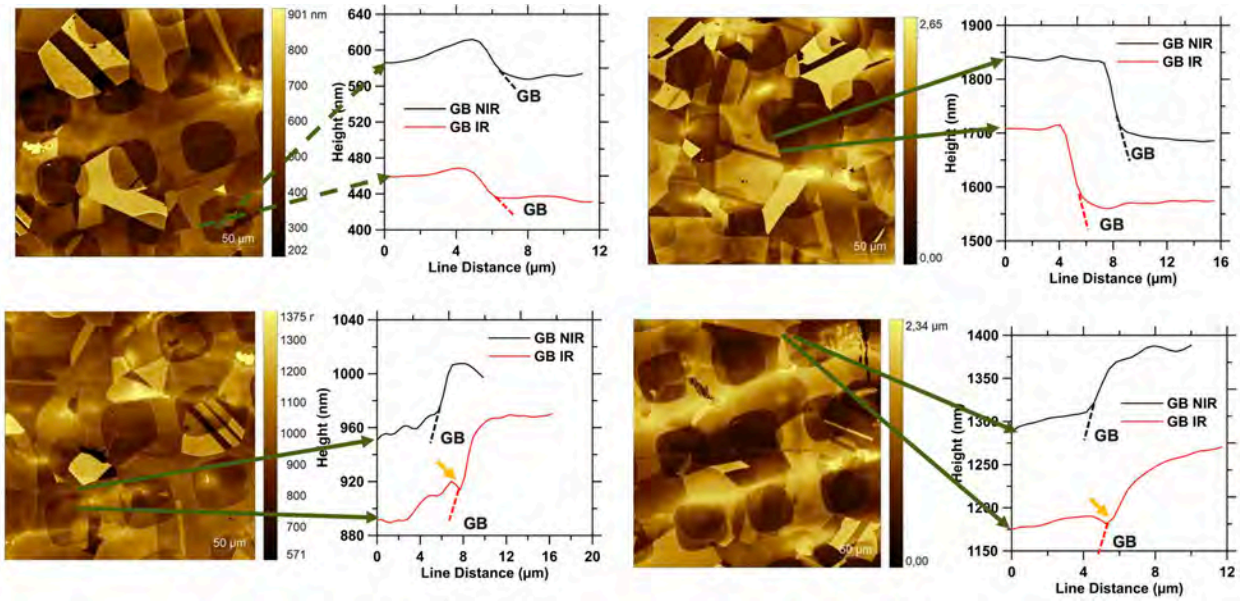

Figure 33 VSI topographical images and surface height line profiles across irradiated and non-irradiated grain boundaries.

4. Summary and conclusions

In summary, we have developed an electrochemical post-damage examination (Ec-PDE) approach to understand and elaborate the underpinnings of IASCC initiation and propagation – across length and time scales. Ec-PDE encompasses multiscale and multimodal approaches to electrochemically examine the interplay between irradiation, deformation, and corrosion. Our results show that deformation and irradiation induced alterations of microstructures can elevate the steel's corrosion tendency, which can be attributed to lattice distortion and disruption of surface oxide films. Both deformation- and irradiation-induced damage similarly reduce corrosion impedance. The measured corrosion rate and surface impedance are quantitatively correlated with the extent and magnitude of strain concentrations and irradiation dose (i.e., dpa). Because of its ability to reveal corrosion activity at micro-to-macro scales, the methodology developed herein can be potentially utilized to predict SCC and IASCC susceptibilities while accommodating both the complex geometries, and diversity of materials used in nuclear components. More importantly, the fast turnaround times of the techniques allow agile adaptation for continuously evolving reactor designs, thereby providing a means for accurate and high-throughput corrosion evaluations, and screening of the microstructural heterogeneities and alternations that can cause the degradation of current/new alloy materials.

5. References

(1) Suter, T.; Böhni, H. A New Microelectrochemical Method to Study Pit Initiation on Stainless Steels. *Electrochimica Acta* **1997**, *42* (20–22), 3275–3280.

(2) Grandy, L.; Mauzeroll, J. Localising the Electrochemistry of Corrosion Fatigue. *Current Opinion in Colloid & Interface Science* **2022**, *61*, 101628.

(3) Bard, A. J.; Mirkin, M. V. *Scanning Electrochemical Microscopy*; CRC Press, 2012.

(4) Gateman, S. M.; Halimi, I.; Costa Nascimento, A. R.; Lacasse, R.; Schulz, R.; Moreau, C.; Chromik, R.; Mauzeroll, J. Using Macro and Micro Electrochemical Methods to Understand the Corrosion Behavior of Stainless Steel Thermal Spray Coatings. *npj Mater Degrad* **2019**, *3* (1), 1–9. https://doi.org/10.1038/s41529-019-0087-0.

(5) Yule, L. C.; Shkirskiy, V.; Aarons, J.; West, G.; Shollock, B. A.; Bentley, C. L.; Unwin, P. R. Nanoscale Electrochemical Visualization of Grain-Dependent Anodic Iron Dissolution from Low Carbon Steel. *Electrochimica Acta* **2020**, *332*, 135267. https://doi.org/10.1016/j.electacta.2019.135267.

(6) Yule, L. C.; Shkirskiy, V.; Aarons, J.; West, G.; Bentley, C. L.; Shollock, B. A.; Unwin, P. R. Nanoscale Active Sites for the Hydrogen Evolution Reaction on Low Carbon Steel. *J. Phys. Chem. C* **2019**, *123* (39), 24146–24155. https://doi.org/10.1021/acs.jpcc.9b07216.

(7) Chen, X.; Gussev, M.; Balonis, M.; Bauchy, M.; Sant, G. Emergence of Micro-Galvanic Corrosion in Plastically Deformed Austenitic Stainless Steels. *Materials & Design* **2021**, 109614.

(8) Sidane, D.; Devos, O.; Puiggali, M.; Touzet, M.; Tribollet, B.; Vivier, V. Electrochemical Characterization of a Mechanically Stressed Passive Layer. *Electrochemistry Communications* **2011**, *13* (12), 1361–1364. https://doi.org/10.1016/j.elecom.2011.08.010.

(9) Sun, P.; Liu, Z.; Yu, H.; Mirkin, M. V. Effect of Mechanical Stress on the Kinetics of Heterogeneous Electron Transfer. *Langmuir* **2008**, *24* (18), 9941–9944. https://doi.org/10.1021/la801009f.

(10) Yazdanpanah, A.; Franceschi, M.; Revilla, R. I.; Khademzadeh, S.; De Graeve, I.; Dabalà, M. Revealing the Stress Corrosion Cracking Initiation Mechanism of Alloy 718 Prepared by Laser Powder Bed Fusion Assessed by Microcapillary Method. *Corrosion Science* **2022**, *208*, 110642. https://doi.org/10.1016/j.corsci.2022.110642.

(11) Yazdanpanah, A.; Pezzato, L.; Dabalà, M. Stress Corrosion Cracking of AISI 304 under Chromium Variation within the Standard Limits: Failure Analysis Implementing Microcapillary Method. *Engineering Failure Analysis* **2022**, *142*, 106797. https://doi.org/10.1016/j.engfailanal.2022.106797.

(12) Was, G. S. *Fundamentals of Radiation Materials Science: Metals and Alloys*; Springer, 2016.

(13) Deng, P.; Peng, Q.; Han, E.-H.; Ke, W.; Sun, C.; Jiao, Z. Effect of Irradiation on Corrosion of 304 Nuclear Grade Stainless Steel in Simulated PWR Primary Water. *Corrosion Science* **2017**, *127*, 91–100.

(14) Birtcher, R. C.; Kirk, M. A.; Furuya, K.; Lumpkin, G. R.; Ruault, M. O. In Situ Transmission Electron Microscopy Investigation of Radiation Effects. *Journal of materials research* **2005**, *20* (7), 1654–1683.

(15) Kaoumi, D.; Liu, J. Deformation Induced Martensitic Transformation in 304 Austenitic Stainless Steel: In-Situ vs. Ex-Situ Transmission Electron Microscopy Characterization. *Materials Science and Engineering: A* **2018**, *715*, 73–82.

(16) Hirst, C. A.; Connick, R. C.; Abel, L.; Carter, K.; Lowder, S.; Cao, P.; Short, M. P. Stored Energy as a Measurable Unit of Radiation Damage in Materials. *Energy Harvesting Footwear* 73.

(17) El-Tahawy, M.; Huang, Y.; Um, T.; Choe, H.; Lábár, J. L.; Langdon, T. G.; Gubicza, J. Stored Energy in Ultrafine-Grained 316L Stainless Steel Processed by High-Pressure Torsion. *Journal of Materials Research and Technology* **2017**, *6* (4), 339–347.

(18) Gussev, M. N.; Howard, R. H.; Terrani, K. A.; Field, K. G. Sub-Size Tensile Specimen Design for in-Reactor Irradiation and Post-Irradiation Testing. *Nuclear Engineering and Design* **2017**, *320*, 298–308.
(19) Gussev, M.; Busby, J.; Field, K.; Sokolov, M.; Gray, S. Role of Scale Factor during Tensile Testing of Small Specimens. In *Small Specimen Test Techniques: 6th Volume*; ASTM International, 2015.
(20) Ziegler, J. F. SRIM-2003. *Nuclear instruments and methods in physics research section B: Beam interactions with materials and atoms* **2004**, *219*, 1027–1036.
(21) Fruzzetti, K. Pressurized Water Reactor Primary Water Chemistry Guidelines-Revision 6. *EPRI, Palo Alto, CA, USA* **2007**.
(22) Nečas, D.; Klapetek, P. Gwyddion: An Open-Source Software for SPM Data Analysis. *Open Physics* **2012**, *10* (1), 181–188. https://doi.org/10.2478/s11534-011-0096-2.
(23) Was, G. S.; Farkas, D.; Robertson, I. M. Micromechanics of Dislocation Channeling in Intergranular Stress Corrosion Crack Nucleation. *Current Opinion in Solid State and Materials Science* **2012**, *16* (3), 134–142.
(24) Johnson, D. C.; Kuhr, B.; Farkas, D.; Was, G. S. Quantitative Linkage between the Stress at Dislocation Channel–Grain Boundary Interaction Sites and Irradiation Assisted Stress Corrosion Crack Initiation. *Acta Materialia* **2019**, *170*, 166–175.
(25) Chimi, Y.; Kitsunai, Y.; Kasahara, S.; Chatani, K.; Koshiishi, M.; Nishiyama, Y. Correlation between Locally Deformed Structure and Oxide Film Properties in Austenitic Stainless Steel Irradiated with Neutrons. *Journal of Nuclear Materials* **2016**, *475*, 71–80.
(26) Deng, P.; Peng, Q.; Han, E.-H.; Ke, W.; Sun, C. Proton Irradiation Assisted Localized Corrosion and Stress Corrosion Cracking in 304 Nuclear Grade Stainless Steel in Simulated Primary PWR Water. *Journal of Materials Science & Technology* **2021**, *65*, 61–71.

Page intentionally left blank